SESR-based Identification of Flash Drought and Multivariate Drought Risk Probability Assessment in the Pearl River Basin, China

Bei Chen
Jinan University
Chuanhao Wu (wuch0907@jnu.edu.cn)
Jinan University
Pat J.-F. Yeh
Jinan University
Jiayun Li
Jinan University
Wenhan Lv
Jinan University
Jin Zhao
Jinan University

Research Article

Keywords: flash drought, SESR, Copula, joint return period, Pearl River basin

Posted Date: November 1st, 2021

DOI: https://doi.org/10.21203/rs.3.rs-946601/v1

SESR-based identification of flash drought and multivariate drought risk probability assessment in the Pearl River basin, China

Bei Chen[a], Chuanhao Wu[a]*, Pat J.-F. Yeh[b], Jiayun Li[a], Wenhan Lv[c], Jin Zhao[d]

[a] Department of Ecology and Hydrobiology, Jinan University, Guangzhou 510632, China.

[b] Discipline of Civil Engineering, School of Engineering, Monash University, Malaysia Campus, Malaysia.

[c] School of Water Resources and Environment, China University of Geosciences, Beijing, 100083, China.

[d] Haihe River, Huaihe River and Xiaoqinghe River Basin Water Conservancy Management and Service Center of Shandong Province, Jinan, 250014, China.

Author for correspondence

Chuanhao Wu (wuch0907@jnu.edu.cn)

Department of Ecology and Hydrobiology, Jinan University, Guangzhou 510632, China.

Abstract

Flash drought (FD) is characterized by the rapid onset and development of drought conditions. It usually occurs during the growing seasons, causing more severe impacts on agriculture and society than the slowly-evolving droughts. Based on the Standard Evaporative Stress Ratio (SESR), this study presents an assessment of the spatio-temporal variability of the joint return periods of FD characteristics in the Pearl River basin (PRB), southern China. Three FD characteristics (i.e., duration *D*, intensity *I*, peak *P*) are extracted at each $0.25^{o}\times0.25^{o}$ grid point over the PRB by the Runs theory. Four marginal distribution functions (Gamma, Exponential, Generalized Extreme Value and Lognormal) are used to fit FD characteristics, while three Archimedean Copula functions (Clayton, Frank and Gumbel) are used for generating the joint distributions of various paired FD characteristics. The results indicate that Lognormal is the best-fitted marginal distribution function of FD characteristics in most parts of PRB, while Frank and Clayton are the best-fitted Copula of the joint PDFs of three pairs of FD characteristics in most parts of PRB. During 1953–2013, the FD events are more frequent in eastern PRB (> 40 events) than western PRB (<10 events), and larger FD characteristics (*D* and *I*) are also found in eastern PRB than western PRB. The return period of each FD characteristic is smaller in eastern PRB than western PRB, leading to smaller joint return periods of three paired FD characteristics (*D-I*, *D-P*, *P-I*) in eastern PRB than western PRB. Overall, our results suggest that the risk of

FD is gradually increased from the west to the east of the PRB.

Key words:

flash drought; SESR; Copula; joint return period; Pearl River basin

1. Introduction

Drought refers to the phenomenon that water availability is in a prolonged deficit lasting for months or years (Ma et al. 2013; Mishra and Singh 2010; Xu et al. 2015). It is a recurrent, inevitable and devastating natural disaster causing significant loss to agriculture, ecology, and social economy (Allen et al. 2010). Global warming increases atmospheric evapotranspiration (ET) demand and leads to uneven distribution of precipitation, triggering frequent drought events in many regions of the world in recent years (Allan et al. 2008; Rahmstorf and Coumou 2011; Tomas-Burguera 2020; Vicente-Serrano 2016). Moreover, drought is expected to become more frequent and more intensity with greater negative impacts under the background of uncertain water supplies, increasing water demand and rapid population growth (Fontaine and Steinemann 2009; Qu et al. 2018; Xia and Wei 2016; Yan et al. 2016; Yin et al. 2015; Trenberth et al. 2014).

Recently, a new type of rapidly developing drought, flash drought (FD), has been receiving increasing attention from the scientific community. The onset and development of FD usually occur rapidly when extreme atmospheric anomalies (e.g., rainfall deficit and high surface temperature) persist for several days or weeks (Christian et al. 2019; Otkin et al. 2018). FD is most likely to occur in regions with dense vegetation during the growing seasons (Otkin et al. 2018; Wang et al. 2016). As FD is distinguished by its unusually rapid intensification, there is no early warning for FD, potentially causing more severe impacts on agriculture and society than the slowly-evolving droughts (Ford et al. 2015; Otkin et al. 2018). Several alternative definitions of FD have been developed in recent years, and they generally can be classified into two types: one is based on the duration (*D*) (Mo and Lettenmaier 2015, 2016), and the other is based on the rapid intensification rate (Ford 2017; Liu et al. 2020; Otkin et al. 2018). In addition, a variety of indices have also been developed to identify the occurrence of FD, including the rapid change index (RCI, Otkin et al. 2015), the Evaporative Stress Index (ESI) (Otkin et al. 2014), the Standard Evaporative Stress Ratio (SESR) (Christian et al. 2019), and the Standardized Evapotranspiration Deficit Index (SEDI) (Li et al. 2020). These metrics are based on the assumption that vegetation pressure is the key driving force of the occurrence of FD, therefore they are more suitable for the densely vegetation regions (Osman et al. 2021). More recently, Christian et al. (2019) developed an objective percentile-based methodology for identifying FD by using the SESR, which is a standardized form of the ratio between ET and potential evapotranspiration (PET). The SESR-based method not only considers the vegetative impacts of FD, but also reflects the dynamic changes and the rapid intensification of FD. In this study, the SESR-based method will be used to identify the occurrence of FD.

Drought characteristics are considered essential elements of water resources and drought management. Drought condition can be commonly characterized by multi-dimensional drought characteristics, such as *D*, intensity (*I*), peak (*P*) and frequency (Dracup et al. 1980). Single drought characteristic variable cannot fully reflect the authenticity of drought events, since different drought characteristics are interdependent (Ayantobo et al. 2018; Shiau 2006, 2009; Sharma and Goyal 2020). Therefore, different drought characteristics as well as their correlation structures and mutual impacts need to be examined together for providing accurate drought assessment (Nabaei et al. 2019; Wu et al. 2021). Most multivariate distributions are currently derived from univariate distributions, which require the same edge distributions of the variables, making the assessment less accurate (Salvadori and Michele 2004). By contrast, the copula method directly simulates the multivariate distribution of multiple random variables, providing a theoretical framework for the multivariate frequency analysis of various variables (Sklar 1959). In the past decade, the copula method has widely used in the multivariate frequency analysis of drought characteristics (Jha et al. 2019, 2020; Lee et al. 2013; Xu et al. 2015; Wu et al. 2021; Zhang et al. 2013), precipitation, runoff and flood (Wee and Shitan 2013; Renard and Lang 2007), and other hydro-meteorological variables like soil moisture, temperature, and sea level (Das and Maity 2015; Rana et al. 2017; Zhang et al. 2007). With this in mind, this study will apply the copula method to present basin-scale analysis of the joint return periods of the paired FD characteristics.

The Pearl River basin (PRB) is the largest basin in southern China, characterized by developed economy and agriculture, dense cities, large population, and farming areas. The climate of PRB is dominated by humid subtropical climate, mainly influenced by the East Asian monsoon (Zhang et al. 2019). Under global warming, the PRB is vulnerable to severe drought since the 1970s (Fischer et al. 2012; Zhang et al. 2013), including more frequent FDs in PRB in recent years (Wang et al. 2016; Wang and

Yuan, 2018; Yuan et al. 2019; Zhang et al. 2019; Zhu et al. 2021). Although some advances have been recently devoted to the analysis of FD in PRB (Wang and Yuan, 2021; Zhang et al. 2019), most of them are only based on the soil moisture decline method, which cannot fully reflect the dynamic changes and the rapid intensification of FD. In addition, to the best of our knowledge, the risk assessment of FD has not yet been conducted in PRB. A systematic spatio-temporal risk assessment of FD events would promote our understanding of the evolution of FD and provide new insights for the implementation of FD forecasting and early warning systems in PRB.

Based on the SESR-based method developed by Christian et al. (2019), this study aims to quantitatively evaluate the spatio-temporal variability of the joint return period of FD characteristics in PRB by using the copula-based models. Particularly, three FD characteristics (i.e., D, I and P) computed based on the SESR are extracted at each 0.25°×0.25° grid point over the PRB. Four marginal distribution functions (Gamma, Exponential, Generalized Extreme Value and Lognormal) are used to fit D, I and P, while three Archimedean Copula functions (Clayton, Frank and Gumbel) are used for generating the joint distributions of various paired FD characteristics. The best-fitted marginal distribution for each drought characteristic and the goodness fitting copula functions are selected based on the root-mean-square error (RMSE) and the Kolmogorov-Smirnov (K-S) test (Kolmogorov 1933; Smirnov 1948). In the following, section 2 introduces the study area. In section 3, the detailed introductions of dataset, definition of FD and drought characteristics, and analysis methods (Mann-Kendall trend test, marginal distribution functions and Copula functions) are provided. Results and discussion are presented in sections 4 and 5, respectively. The main findings drawn from this study are summarized in section 6.

2. Study area

The PRB (102° 14′ to 115° 53′E and 21° 31′ to 26° 49′N) is composed of the West River basin (WRB), the North River basin (NRB), the East River basin (ERB) and the Pearl River Delta (PRD), with a total drainage area of 4.42×10^5 km^2 (Fig. 1). The PRB has a concentrated population and developed industry and agriculture, with a high meteorological disaster vulnerability (Liu et al. 2012). The basin is dominated by the tropical and subtropical monsoon climate, with annual mean temperature ranging from 14 to 22 ℃, and annual mean precipitation decreasing from 2200 mm in the east to 1200 mm in the west. The precipitation of PRB has an uneven intra-annual distribution, with 60–70% of annual precipitation occurring during April-September (Tang et al. 2015). Due to global warming, PRB is vulnerable to drought and short-term concurrent hot and dry extreme events in recent years (Zhang et al. 2019).

3. Dataset and Methodology

3.1 Dataset

Atmospheric reanalysis makes a perfect combination of observations and earth system models, and provides spatiotemporal estimates about the earth's atmosphere and land surface variables (Koster 2019). Global Land Data Assimilation System (GLDAS) aims to utilize advanced land surface modeling and data assimilation techniques to obtain reliable estimates of land surface states and fluxes (Ji et al. 2015; Park and

Choi 2015; Rodell et al. 2004). The high-quality, global land surface fields provided by the GLDAS have been widely used in weather and climate prediction, water resources applications, and water cycle investigations (Bi et al. 2016; Yuan et al. 2018). In this study, the long-term (1953-2013) daily ET data over the PRB with a spatial resolution of 0.25° were driven from the GLDAS-2.0 forcing data (https://ldas.gsfc.nasa.gov/).

Observed daily meteorological data, including precipitation, mean temperature, maximum and minimum temperature, air pressure, vapor pressure, sunshine duration, and wind speed, spanning the period 1953-2013 were driven from 65 meteorological stations over the PRB (see Fig. 1) provided by the National Meteorological Information Center (http://data.cma.cn). Based on the meteorological observation data, daily PET was calculated by using the FAO-56 Penman-Monteith method (Mahrt and Michael 1984; Penman 1948). To match the spatial scale of GLDAS-2.0 data, the PET data was interpolated to 0.25° spatial resolution over the PRB by using the bilinear interpolation.

3.2 FD identification

Christian et al. (2019) developed an objective percentile-based methodology for identifying the occurrence of FD using the SESR and changes in SESR. This method not only considers the vegetative impacts of FD, but also quantifies the rapid rate of drought intensification. Specifically, the FD identification is based on the evaporative stress ratio (ESR), which can be expressed as follows:

$$\mathrm{ESR} = \frac{\mathrm{ET}}{\mathrm{PET}} \tag{1}$$

where ESR ranges from 0 to approximately 1. The value of ESR is inversely proportional to the amount of evaporative stress on the environment (Christian et al. 2019).

For the FD identification, the standardized ESR (i.e., SESR) and the standardized change in SESR are computed at each grid point:

$$\mathrm{SESR}_{ijp} = \frac{\mathrm{ESR}_{ijp} - \overline{\mathrm{ESR}_{ijp}}}{\sigma_{\mathrm{ESR}_{ijp}}} \tag{2a}$$

$$\left(\Delta\mathrm{SESR}_{ijp}\right)_z = \frac{\Delta\mathrm{SESR}_{ijp} - \overline{\Delta\mathrm{SESR}_{ijp}}}{\sigma_{\Delta\mathrm{SESR}_{ijp}}} \tag{2b}$$

where SESR_{ijp} and $\left(\Delta\mathrm{SESR}_{ijp}\right)_z$ represent the z-score of ESR and change in SESR, respectively, for a specific pentad (*p*) at a specific grid point (*i*, *j*). ΔSESR represents the rapid intensification of FD in time at each grid point.

Taking into account the frequent characteristics of high-temperature heat waves in PRB (Zhang et al. 2019) and according to Christian et al. (2019), the following four criteria are considered to identify the occurrence of FD events in PRB: (1) a minimum length of 3 SESR changes (ΔSESR), equivalent to a length of four pentads (20 days), (2) the final SESR should be below the 20th percentile of SESR values, (3) ΔSESR should be below the 40th percentile between two pentads and no more one ΔSESR is above the 40th percentile following a ΔSESR, and (4) the mean change in SESR throughout the whole FD should be less than the 25th percentile of the changes in

SESR. The first two criteria address the effects of FDs on environment, while the latter two criteria emphasize the rapid intensification of FD. More detailed explanations of the four criteria can be referred to Christian et al. (2019). In this study, the minimum length of 20 days (four pentads) for criterion 1 is selected according to the frequent characteristics of high-temperature heat waves in PRB (Zhang et al. 2019). Based on the above criteria, the occurrence of FD events is identified at each grid point over the PRB during the vegetative growing season (April-November) for the period 1953-2013.

Based on the Runs theory (Yevjevich 1967), three FD characteristics (*D, I, P*) are extracted from the FD events at each grid point over the PRB. *D* refers to the total pentads for a FD event. *P* is defined as the absolute value of the minimum SESR during a FD event. *I* is the absolute mean change in SESR throughout the whole FD event, which reflects uncontrollable and dramatic changes of environment.

3.3 Mann-Kendall trend test

The Mann-Kendall (M-K) test is a non-parametric statistical method for testing the trend of hydrometeorological data (Dawood 2017; Kendall 1975; Mann 1945). The M-K method has the advantages of not assuming any distribution forms for the data and not being affected by interference from outliers, and is widely used for detecting the significance of long-term trends in hydrometeorological variables (Gocic and Trajkovic 2013; Li et al. 2021; Mekonen and Berlie 2020; Wu et al. 2018). In this study, we apply the M-K method to detect the statistical significance of the trends in

FD characteristics (D, I and P) at the 5% significance level (a = 0.05). The non-parametric trend slope estimator method (Sen 1968) is used to estimate trend magnitudes in FD characteristics.

3.4 Marginal distribution

Four different probability distribution functions (PDFs), namely gamma (GAM), exponential (EXP), generalized extreme value (GEV) and lognormal distribution (LOG), are used to fit FD characteristics (Table 1). We choose these PDFs, because they are widely used in estimating the marginal probability distributions of meteorological drought characteristics (Nabaei et al. 2019; Wu et al. 2021). The parameters of each PDF are estimated using the maximum likelihood estimation method (Xu et al. 2015). The RMSE and K-S test are used for goodness of fit tests to select the best marginal distribution at the 95% significance level, that is, the optimal marginal distribution is selected after passing the K-S test and having the smallest RMSE (Wu et al. 2021). The formulas of the K-S test are expressed as follows:

$$K_n(x) = \frac{1}{n}\sum_{i=1}^{n} I_{[-\infty,x]}(X_i) \tag{3a}$$

$$I_{[-\infty,x]}(X_i) = \begin{cases} 1, X_i \le x \\ 0, X_i > x \end{cases} \tag{3b}$$

where $K_n(x)$ is the K-S statistic and $I_{[-\infty,x]}$ is an indicator function ranging from 0 to 1.

3.5 Copula functions

Copula is a joint function that connects two or more marginal distribution functions ($F_X(x)F_Y(y)$) from a joint distribution function ($F_{X,Y}(x,y)$), which describes the probability that the two or more variables are equal to or less than a given value (Sklar 1959). The general form of copula is expressed as (Nelsen 2006):

$$F_{X,Y}(x,y) = C[F_X(x), F_Y(y)] = C[u, v] \tag{4}$$

where *u* and *v* are the marginal distribution functions of *X* and *Y*, respectively. The copula functions can be classified to three forms: elliptical, Archimedean, and quadratic, and among them Archimedean copulas are widely used for hydro-meteorological analyses (Bisht et al. 2019; Thilakarathne and Sridhar 2017; Wu et al. 2021). In this study, three common Archimedean copula functions, including Clayton, Frank and Gumbel copulas (Table 2), are used to construct the joint distribution of three pairs of FD characteristics (*D-I, I-P, D-P*) at each grid over the PRB. The K-S test and RMSE are used to assess the goodness fitting of copula functions.

3.6 Return period

For a single variable (*X*) equal to or greater than a given value (*x*), univariate return period $T(x)$ can be calculated as:

$$T(x) = \frac{N}{n[1-F(x)]} \tag{5}$$

where N is the length of the study period (i.e., 61-yr in this study), n is total number of FD events, and $F(x)$ is the marginal distribution of FD characteristic.

In this study, two different joint probabilities ($P_{x\vee y}$ and $P_{x\wedge y}$) of three pairs of FD characteristics are considered (Shiau 2006; Nabaei et al. 2019):

$$P_{x\vee y} = P(X > x \ \ or \ \ Y > y) = 1 - C\big(F_X(x), F_Y(y)\big) = 1 - C(u, v) \tag{6a}$$

$$P_{x\wedge y} = P(X > x, Y > y) = 1 - F_X(x) - F_Y(y) + C\big(F_X(x), F_Y(y)\big) = 1 - u - v + C(u, v) \tag{6b}$$

where the symbol ∨ denotes “union” (“or”) and ∧ denotes “intersection” (“and”). The corresponding return periods of $P_{x\vee y}$ (union return period, T_o) and $P_{x\wedge y}$ (co-occurrence return period, T_a) are expressed as follows:

$$T_o = \frac{N}{n[1 - C(u,v)]} \tag{7a}$$

$$T_a = \frac{N}{n[1 - u - v + C(u,v)]} \tag{7b}$$

where u and v are the marginal distributions of FD characteristics, and $C(u, v)$ is the joint distribution of the pairs of FD characteristics.

4. Results

4.1 Spatial and temporal trends in FD characteristics

The spatial distributions of mean D, I and P as well as the frequency of FD events during 1953-2013 are displayed in Fig. 2. It is shown that the frequency of FD (events) is less than 20 in most parts of PRB and tends to decrease from the eastern (> 50) to western (<10) regions (Fig. 2a). D is less than 22 days in almost the whole study basin (except for the PRD and the downstream of ERB, Fig. 2b). Similarly, I tends to decrease from the east (> 0.7) to the west (~ 0.5) regions (Fig. 2c). The range of P is 0.94 ~1.38 over the PRB (Fig. 2d), and smaller (larger) P is found in the midstream of WRB and upstream of NRB (western WRB).

Fig. 3 displays the spatial distributions of the trend magnitudes in *D*, *I* and *P* over the study area during the period 1953-2013. As shown in Fig. 3a, a substantial spatial difference in the trend magnitudes of *D* is found across the PRB (Fig. 3a). A decreasing trend in *D* is observed in most parts of PRB, with a significant decreasing trend ($a < 0.05$) in the downstream of NRB and PRD. In contrast, an increasing trend (not significant) in *D* is found in the upper and middle reaches of WRB, the upstream of NRB and some parts of southeastern PRB (Fig. 3a). For *I*, a significant decreasing trend ($a < 0.05$) is concentrated in the middle and lower reaches of WRB and the upstream of NRB (down to 3.1). In contrast, the significant increasing trend appears only in western WRB and southern NRB (up to 2.39, Fig. 3b), which is generally the opposite of the increasing trend of *D* (Fig. 3a). *P* shows an increasing trend mainly in the upstream and downstream of WRB and western NRB (up to 3.8), while the decreasing trend is scattered in the northern and southern parts of middle WRB as well as the downstream of NRB (the largest decline is > 2.8, Fig. 3c).

4.2 Selection of marginal distributions and bivariate Copulas

The GAM, EXP, GEV and LOG are used to fit the marginal distributions of *D*, *I* and *P* at each grid over PRB. The Clayton, Frank and Gumbel are used to fit the joint probability distributions of *D-I*, *D-P*, and *P-I*. The best marginal distribution and Copula at each grid are selected when it passes the K-S test and has the smallest RMSE. The distributions of the best-fitted marginal distribution of each FD characteristic determined by the RMSE and K-S test are displayed in Fig. 4. It is found that LOG is the best-fitted marginal distribution function of *D*, *I* and *P* for most of PRB, accounting for 88%, 53% and 70% of the total grids, respectively. For *D*, the percentage of grids identified by the EXP distribution is approximately 10%, while for *I* and *V* the percentage of grids identified by the GEV distribution is approximately 47% and 27%, respectively. In contrast, for *D* (*I* and *V*), almost no grids are identified by the GEV (EXP) distribution. In addition, for all FD characteristics, almost no grids are identified by the GAM distribution (except for some grids for *P*, Fig. 4c). Overall, at the basin scale, GEV is the best-fitted marginal distribution function of *P* in ERB, while LOG is the best-fitted marginal distribution of all FD characteristics in WRB and NRB.

The spatial distributions of the best-fitted Copula functions of *D-I*, *D-P*, and *P-I* are displayed in Fig. 4d~f. As shown, the best-fitted Copula functions of three pairs of FD characteristics can be identified in all the grids over the PRB. Frank, Clayton, and Gumbel are the best-fitted Copula functions accounting for 61.4%, 31.2%, and 7.4% for the joint *D-I* PDFs, 67.3%, 24.5%, and 8.2% for the joint *D-P* PDFs, and 67.3%, 28.5%, and 4.2% for the joint *P-I* PDFs over the PRB. In contrast, very few grids are identified by the Gumbel function for all three pairs of FD characteristics.

4.3 Joint PDF of FD characteristics

The joint PDF at each grid point over the PRB is constructed using the best fitted marginal distribution and copula function. The two-dimensional joint PDFs of *D-I, D-*

P and P-I in WRB, NRB and ERB are displayed in Fig. 5. As seen, when $D < 20$ days and $I < 0.5$, the joint PDF of D-I can be neglected in all basins. Similarly, the joint PDF of $D < 20$ days and $P < 0.7$, 0.87 and 0.92 also tends to be neglected in WRB, NRB and ERB, respectively. In contrast, when D increases from 20 to 40 days and I increases from 0.5 to 1, the joint PDF of D-I sharply increases close to 1 in all basins. When D increases from 20 to 40 days and P increases from 0.7 to 2, 0.87 to 2 and 0.92 to 2 in WRB, NRB and ERB, respectively, the joint PDF of D-P increases close to 1. Similarly, when I increases from 0.5 to 1 and P increases from 0.7 to 2, 0.87 to 2 and 0.92 to 2, the joint PDF of I-P increases close to 1 in WRB, NRB and ERB, respectively. However, the increasing rate of joint PDF tends to decrease when $D > 28$ days and $P > 1.4$ in WRB, NRB and ERB. Also, the increasing rate of joint PDF tends to decrease when $D > 28$ days and $I > 0.68$, 0.79, 0.82 respectively in WRB, NRB and ERB.

It can be found by comparison that the joint PDFs of D-I, D-P and P-I tend to be 'fatter' in WRB and NRB than in ERB, suggesting a higher risk of FD in ERB than in WRB and NRB. This is supported by Table 3, showing that the design values of D corresponding to the same return periods (10, 20, 50, and 100a) are generally the largest in ERB, followed by WRB and NRB. Similarly, the design values of P and I corresponding to the same return periods are the largest in ERB, followed by NRB and WRB.

4.4 Geographic pattern of T_o

The contour maps of T_o of *D-I, D-P,* and *P-I* in WRB (the first row), NRB (the second row), and ERB (the third row) are displayed in Fig. 6. As shown, for a certain *I* and *P*, the T_o of *D-I* and *D-P* is the largest in WRB, followed by NRB and ERB, suggesting a higher probability of a smaller *D* in WRB than in the other two basins, a consistent finding with that in Fig. 2b. For a certain *I* and *P*, the T_o of *I-P* is also the largest in WRB, followed by NRB and ERB, suggesting a higher probability of smaller *I* and *P* in WRB than in the other two basins, a consistent finding with that in Fig. 2c and d. It is also found that the T_o tends to increase slowly (< 50-yr) and then fast (>100-yr) with the increasing *D, I* and *P* in all three basins.

Four different design values of *D*, *I* and *P* corresponding to different univariate return periods (10, 20, 50, and 100a) are used to compute the T_o of *D-I*, *D-P*, and *P-I* in WRB, NRB, and ERB (Table 3). For the same return periods, the T_o of *D-I* and *D-P* is the largest in WRB, followed by NRB and ERB, while the T_o of *P-I* is the largest in NRB, followed by WRB and ERB. In addition, the T_o of *P-I* is larger than that of *D-I* and *D-P* in all basins.

Three specified thresholds of *D* (*D1*: 20d, *D2*: 25d, *D3*: 30d), *I* (*I1*: 25th, *I2*: 50th, *I3*: 75th percentile), and *P* (*I1*: 25th, *I2*: 50th, *I3*: 75th percentile) are used to calculate the T_o at each grid point over the PRB. The spatial distributions of the T_o of *D1-I1, D2-I2, D3-I3*, *D1-P1, D2-P2, D3-P3, I1-P1, I2-P2* and *I3-P3* are displayed in Fig. 7. As shown, the T_o of *D1-I1, D2-I2, D1-P1, D2-P2, I1-P1* and *I2-P2* is less than 10a in most parts of western PRB and less than 5a in eastern PRB. The T_o of *D3-I3* is in the range of 30~300a in southern ERB and PRD, and is greater than 300a in most of NRB and WRB (Fig. 7c). The T_o of *D3-P3* and *P3-I3* is less than 5a in ERB and PRD, and less than 30a in most of WRB (Fig. 7f), which is significantly smaller than the T_o of *D3-I3* (Fig. 7c).

4.5 Geographic pattern of T_a

The T_a is calculated at the basin scale by equation (7b). The contour maps of T_a of *D-I, D-P,* and *P-I* in three basins (WRB, NRB, and ERB) are displayed in Fig. 8. For a certain *D*, *I* and *P*, the T_a of *D-I*, *D-P,* and *P-I* is the smallest in ERB, suggesting a higher risk of FD in ERB compared with the other two basins. The T_a of *D-I* and *D-P* is smaller (larger) in NRB than WRB when *D* is less (larger) than 21 days, while the T_a of *P-I* is larger in WRB than NRB. The design values of FD characteristics and the corresponding T_a in three basins are shown in Table 3. For the same return periods (10, 20, 50 and 100a), the T_a of *D-I* is the largest in NRB, followed by ERB and WRB, the T_a of *D-P* is the largest in ERB, followed by NRB and WRB, and the T_a of *P-I* is the largest in ERB, followed by WRB and NRB. In addition, the T_a of *D-P* is larger than that of *D-I* and *P-I* in WRB and ERB, while in NRB the T_a of *D-I* is significantly larger than that of *D-P* and *P-I.*

Three specified thresholds of *D* (*D1*: 20d, *D2*: 25d, *D3*: 30d), *I* (*I1*: 25th, *I2*: 50th, *I3*: 75th percentile), and *P* (*I1*: 25th, *I2*: 50th, *I3*: 75th percentile) are used to calculate the T_a at each grid point over the study basin. The spatial distributions of the T_a of *D1-I1,*

D2-I2, D3-I3, *D1-P1, D2-P2, D3-P3, I1-P1, I2-P2* and *I3-P3* are displayed in Fig. 9. As shown in Fig. 9, the T_a of *I1-P1, I2-P2, D1-P1* and *D1-I1* is less than 5a in eastern PRB and larger than 10a in some parts of WRB. The areas with the T_a of *I1-P1, I2-P2, D1-P1* and *D1-I1* less than 5a are decreased in order. For *D2-I2* and *D2-P2* (Fig. 9b and e), the T_a is less than 30a in southeastern PRB, and larger than 300a in most parts of WRB and NRB. For *D3-I3*, *D3-P3* and *I3-P3* (Fig. 9c, f and i), the T_a is larger than 300a in most parts of PRB, and the area with T_a larger than 300a is the largest for *D3-I3*, followed by *D3-P3* and *P3-I3*. In contrast, the T_a of *D3-P3* and *I3-P3* less than 30a is concentrated only in southern PRD, southern ERB, and western and central WRB.

5. Discussion

Based on the GLDAS and observation data, we used four marginal distribution functions (GAM, EXP, GEV, and LOG) and three Archimedean Copulas (Clayton, Gumbel and Frank Copula) to explore the geographic pattern of bidimensional return period (T_o and T_a) of the paired FD characteristics (*D-I*, *D-P* and *P-I*) over the PRB. It was found that different FD characteristics usually follow different statistical distributions, resulting in a large spatial variability in the best-fitted marginal probability distributions of FD characteristics as well as the best-fitted copulas of the paired FD characteristics over the study basin. This is generally consistent with the previous studies on the probability distribution assessment of meteorological drought characteristics at the global (Wu et al. 2021) and regional (Nabaei et al. 2019) scales. Our results suggest that only one or few PDFs (or copula functions) were selected for analysis may lead to inaccurate probability estimates of FD characteristics, because they may not be the best PDFs (or copula functions) of FD characteristics.

The analysis indicates a larger FD characteristic (Fig. 2) as well as a smaller joint return period of FD characteristics in eastern PRB (mainly southern ERB and PRD) (Fig. 7 and 9). In contrast, the smaller FD characteristic (Fig. 2) and larger joint return period of FD characteristics are concentrated in western WRB (Fig. 7 and 9). This suggests a high risk of FD in southern ERB and PRD and a lower risk of FD in western WRB (Fig. 2, 7, and 9). Two key reasons might be responsible for the higher FD risk in eastern PRB (mainly southern ERB and PRD). First, the plain areas in PRD are mainly heavy population and dense cities, in which surface fluxes and ET are highly sensitive to changes in soil moisture (Guo et al. 2006; Wei et al. 2016), easily accelerating the continuous drying of the atmosphere and leading to a decrease in SESR. In addition, the ERB is dominated by agricultural regions, which generally have a shallower root zone and a high rate of ET (soil moisture depletion) with high risk of short-term concurrent hot and dry extremes (Zhang et al. 2019). In contrast, the lower risk of FD in western PRB (mainly western WRB) can be attributed to the high-altitude terrain, where relatively sparse vegetation limits transpiration and causes ET to be restricted (Pielke 2001).

Note that this study is subject to a few limitations. First, for FD identification, the minimum length of 20 days (four pentads) is selected for the whole basin according to the frequent characteristics of high-temperature heat waves in PRB (Zhang et al. 2019). For a certain region, changes in the threshold of the minimum D would affect the number of FD events and the size of FD characteristics. On the other hand, because FD characteristics have strong spatial variability (Fig. 2), it is reasonable to believe that the threshold of the minimum *D* of FD also has a strong spatial variability. Therefore, it would be interesting in future work to explore the sensitivity of the number of FD events and the size of FD characteristics to the threshold of the minimum *D* to determine the most suitable minimum *D* of FD at each grid point over the study basin. In addition, we also found that there are few FD events (less than 10 times) identified in western WRB (Fig. 2a). The relatively small sample size of FD events may not be able to fully characterize the range of FD characteristics, which may lead to inaccurate probability estimates of FD characteristics.

6. Conclusions

Based on the SESR-based method developed by Christian et al (2019), the occurrence of FD events during the period 1953–2013 was identified at each 0.25°×0.25° grid point over the PRB. Three FD characteristics (i.e., duration *D*, intensity *I*, peak *P*) were extracted by the Runs theory. Four marginal distribution functions (Gamma, Exponential, GEV and Lognormal) were used to fit *D*, *I* and *P*, while three Archimedean Copula functions (Clayton, Frank and Gumbel) were used for generating the joint distributions of various paired FD characteristics. The spatio-temporal variability of the two different joint return periods (union return period T_o and co-occurrence return period T_a) of three pairs of FD characteristics (*D-I, D-P* and

I-P) over the PRB was quantitatively assessed using copula-based models. The main findings drawn from this study are summarized as follows.

(1) Different FD characteristics usually follow different statistical distributions, resulting in a large spatial variability in the best-fitted marginal probability distributions of FD characteristics as well as the best-fitted copulas of the paired FD characteristics. Overall, LOG is the best-fitted marginal distribution function of *D*, *I* and *P* for most of PRB, accounting for 88%, 53% and 70% of the total area of PRB, respectively. Frank and Clayton are the best-fitted Copula of the joint PDFs of three pairs of FD characteristics for most of the PRB, accounting for 61.4%~67.3% and 24.5%~28.5% of the total area of PRB, respectively.

(2) During the period 1953–2013, the FD events are more frequent in eastern PRD and southern ERB (> 40 events) than in western WRB (<10 events). Similarly, larger *D* and *I* are observed in PRD and southern ERB, while larger *P* is observed in western WRB and southern ERB. The trend analysis shows that a decreasing trend in *D* is observed in most of PRB (especially PRD). *I* shows a significant decreasing (increasing) trend in the middle and lower reaches of WRB and the upstream of NRB (western WRB and southern NRB), while *P* shows an increasing (decreasing) trend mainly in the downstream of WRB (central WRB and southern NRB).

(3) The return period of *D* is the smallest in ERB, followed by WRB and NRB. The return periods of *P* and *I* are the smallest in ERB, followed by NRB and WRB. The T_o and T_a show generally similar spatial patterns over the PRB, but the magnitude of T_a is

significantly larger than that of T_o. The T_o and T_a of *D-I, D-P,* and *P-I* are both smaller in eastern PRB than western PRB, resulting the highest risk of FD in ERB followed by NRB and WRB.

Declarations

Funding

See **Acknowledgements.**

Acknowledgements

This research was supported by funding from the National Natural Science Foundation of China (Grant No. 51909106, 51879108), the Natural Science Foundation of Guangdong Province, China (Grant No. 2018A030310653), the high-level talent project for the "Pearl River Talent Plan" of Guangdong Province (Grant No. 2017GC010397), and the Youth Innovative Talents Project for Guangdong Colleges and Universities (Grant No. 2017KQNCX010).

Data availability

The daily ET data of the study area were driven from the GLDAS-2.0 forcing data (https://ldas.gsfc.nasa.gov/). The daily meteorological data were provided by the National Meteorological Information Center (http://data.cma.cn).

Code availability

Not applicable.

Authors' contributions

All authors contributed to the study conception and design.

Bei Chen provided the methodology, analyzed the data, wrote the code and the original draft. Chuanhao Wu provided the methodology, funding acquisition, and revised the manuscript. Pat J.-F. Yeh provided the writing guidance and review. Jiayun Li provided the guidance of conceptualization and writing. Wenhan Lv collected the data. Jin Zhao revised the writhing grammer.

Compliance with ethical standards

Conflicts of interest/Competing interests

We have no conflict of interest.

Ethics approval

We confirm that this article is original research and has not been published or presented previously in any journal or conference in any language (in whole or in part).

Consent to participate and consent for publication

We have consent to participate and publish.

References

Allen CD, Macalady AK, Chenchouni H, Bachelet D, McDowell N, et al (2010) A global overview of drought and heat-induced tree mortality reveals emerging climate change risks for forests. For. Ecol. Manag 259(4): 660-684. https://doi.org/10.1016/j.foreco.2009.09.001

Allan RP, Soden BJ (2008) Atmospheric warming and the amplification of precipitation extremes. Science 321(5895): 1481-1484. http://doi.org./10.1126/scince.1160787

Ayantobo OO, Li Y, Song S, Javed T, Yao N (2018) Probabilistic modelling of drought events in China via 2-dimensional joint copula. J. Hydrol 559: 373-391. https://doi.org/10.1016/j.jhydrol.2018.02.022

Bi HY, Ma JW, Zheng WJ, Zeng JY (2016) Comparison of soil moisture in GLDAS model simulations and in situ observations over the Tibetan plateau. J. Geophys. Res. Atmos 121(6): 2658–2678. https://doi.org/10.1002/2015JD024131

Bisht DS, Sridhar V, Mishra A, Chatterjee C, Raghuwanshi NS (2019) Drought characterization over India under projected climate scenario. Int J Climatol 39(4): 1889–1911. https://doi.org/10.1002/joc.5922

Christian JI, Basara JB, Otkin JA, Hunt ED, Wakefield RA (2019) A methodology for flash drought identification: Application of flash drought frequency across the United States. J Hydrometeorol 20(5): 833-846. https://doi.org/10.1175/JHM-D-18-0198.1

Das SK, Maity R (2015) A hydrometeorological approach for probabilistic simulation of monthly soil moisture under bare and crop land conditions. Water Resour. Res 51(4): 2336-2355. https://doi.org/10.1002/2014WR016043

Dawood M (2017) Spatio-statistical analysis of temperature fluctuation using Mann–Kendall and Sen’s slope approach. Clim. Dyn 48 (3-4): 783-797. http://dx.doi.org/10.1007/s00382-016-3110-y

Dracup JA, Lee KS, Paulson EG (1980) On the definition of droughts. Water Resour. Res 16(2): 297-303. https://doi.org/10.1029/WR016i002p00297

Fontaine MM, Steinemann AC (2009) Assessing vulnerability to natural hazards: Impact-based method and application to drought in Washington State. Nat Hazards Rev 10(1): 11-18. https://doi.org/10.1061/(ASCE)1527-6988(2009)10:1(11)

Fischer T, Gemmer M, Su B, Scholten T (2012) Long-term meteorological and hydrological dryness and wetness conditions in the Zhujiang River Basin, South China. Hydrology and Earth System Sciences Discussions, 9(9): 10525-10562.

Ford TW, McRoberts DB, Quiring SM, Hall RE (2015) On the utility of in situ soil moisture observations for flash drought early warning in Oklahoma, USA. Geophys. Res. Lett 42(22): 9790-9798. https://doi.org/10.1002/2015GL066600

Ford TW, Labosier CF (2017) Meteorological conditions associated with the onset of flash drought in the eastern United States. Agric For Meteorol 247: 414-423. https://doi.org/10.1002/2015GL066600

Gocic M, Trajkovic S (2013) Analysis of changes in meteorological variables using Mann-Kendall and Sen’s slope estimator statistical tests in Serbia. Glob Planet Chang 100:172–182. https://doi.org/10.1016/j.gloplacha.2012.10.014

Guo Z, Dirmeyer PA, Koster RD, Bonan G, Chan E, Cox P, et al (2006). GLACE: the global land－atmosphere coupling experiment. Part II: analysis. J Hydrometeorol 7:

611－625. https://doi.org/10.1175/JHM511.1

Jha S, Das J, Goyal MK (2019) Assessment of risk and resilience of terrestrial ecosystem productivity under the influence of extreme climatic conditions over India. Sci. Rep 9(1): 1-12. https://doi.org/10.1038/s41598-019-55067-0

Jha VB, Gujrati A, Singh RP (2020) Copula based analysis of meteorological drought and catchment resilience across Indian river basins. Int J Climatol 41, E1137-E1151. https://doi.org/10.1002/joc.6758

Ji L, Senay GB, Verdin JP (2015) Evaluation of the Global Land Data Assimilation System (GLDAS) air temperature data products. J Hydrometeorol 16(6), 2463–2480. https://doi.org/10.1175/JHM-D-14-0230.1

Kendall MG (1975) Rank correlation methods. 4th edition.

Kolmogorov A (1933) Sulla determinazione empirica di una legge di distribuzione. Giornale dell'Istituto Italiano degli Attuari, 4: 83-91.

Koster RD, Schubert SD, Wang H, Mahanama SP, DeAngelis AM (2019) Flash drought as captured by reanalysis data: Disentangling the contributions of precipitation deficit and excess evapotranspiration. J Hydrometeorol 20(6): 1241-1258. https://doi.org/10.1175/JHM-D-18-0242.1

Lee T, Modarres R, Ouarda TBMJ (2013) Data-based analysis of bivariate copula tail dependence for drought duration and severity. Hydrol Process 27(10): 1454-1463. https://doi.org/10.1002/hyp.9233

Liu LL, Jiang T, Xu JG, Zhai JQ, Luo Y (2012) Responses of hydrological processes to the climate change in the Zhujiang River basin in the 21st century. Adv. Clim. Chang.

Res 3(2): 84-91. https://doi.org/10.3724/SP.J.1248.2012.00084

Li J, Wang ZL, Wu XS, Guo SL, Chen XH (2020) Flash droughts in the Pearl River Basin, China: Observed characteristics and future changes. Sci. Total Environ 707: 136074. https://doi.org/10.1016/j.scitotenv.2019.136074

Liu Y, Zhu Y, Zhang LQ, Ren LL, Yuan F, Yang XL, Jiang SH (2020) Flash drought characterization over China: From a perspective of the rapid intensification rate. Sci. Total Environ, 704. https://doi.org/10.1016/j.scitotenv.2019.135373

Li JY, Wu CH, Xia CA, Yeh PJF, Hu BX, Huang GR (2021) Assessing the responses of hydrological drought to meteorological drought in the Huai River Basin, China. Theoretical and Applied Climatology, 144(3): 1043-1057. https://doi.org/10.1007/s00704-021-03567-3

Mann HB (1945) Nonparametric test against trend. Econometrica: Journal of the econometric society 13(3): 245-259. https://doi.org/10.2307/1907187

Mahrt L, Michael Ek (1984) The Influence of atmospheric stability on potential evaporation. J Appl Meteorol Climatol 23(2): 222-234. https://doi.org/10.1175/1520-0450(1984)023<0222:TIOASO>2.0.CO;2

Ma MW, Song SB, Ren LL, Jiang SH, Song JL (2013) Multivariate drought characteristics using trivariate Gaussian and Student t copulas. Hydrol Process 27(8): 1175-1190. https://doi.org/10.1002/hyp.8432

Mekonen AA, Berlie AB (2020) Spatiotemporal variability and trends of rainfall and temperature in the Northeastern Highlands of Ethiopia. Environ. Earth Sci 6(1): 285–300. https://doi.org/10.1007/s40808-019-00678-9

Mishra AK, Singh VP (2010) A review of drought concepts. Journal of Hydrology, 391(1-2): 202-216. https://doi.org/10.1016/j.jhydrol.2010.07.012

Mo KC, Lettenmaier DP (2015) Heat wave flash droughts in decline. Geophys. Res. Lett 42(8): 2823-2829. https://doi.org/10.1002/2015GL064018

Mo KC, Lettenmaier DP (2016) Precipitation deficit flash droughts over the United States. J Hydrometeorol 17(4): 1169-1184. https://doi.org/10.1175/JHM-D-15-0158.1

Nabaei S, Sharafati, A, Yaseen ZM, Shahid S (2019) Copula based assessment of meteorological drought characteristics: regional investigation of Iran. Agric For Meteorol 276, 107611. https://doi.org/10.1016/j.agrformet.2019.06.010

Nelsen RB (2006) An introduction to copulas, ser. Lect. Notes Stat. Springer, New York.

Osman M, Zaitchik BF, Badr HS, Christian JI, Tadesse T, Otkin JA, Anderson MC (2021) Flash drought onset over the contiguous United States: sensitivity of inventories and trends to quantitative definitions. Hydrol Earth Syst Sci 25(2): 565-581. https://doi.org/10.5194/hess-25-565-2021

Otkin JA, Shafer M, Svoboda M, Wardlow B, Anderson MC (2014) Facilitating the use of drought early warning information through interactions with agricultural stakeholders. Bull Am Meteorol Soc 96(7), 1073-1078. https://doi.org/10.1175/BAMS-D-14-00219.1

Otkin JA, Anderson MC, Hain C, Svoboda M (2015) Using temporal changes in drought indices to generate probabilistic drought intensification forecasts. Journal of Hydrometeorology, 16(1), 88-105. https://doi.org/10.1175/JHM-D-14-0064.1

Otkin JA, Svoboda M, Hunt ED, Ford TW, Andersoson MC, Basara JB (2018) Flash droughts: A review and assessment of the challenges imposed by rapid-onset droughts in the United States. Bull Am Meteorol Soc 99(5): 911-919. https://doi.org/10.1175/BAMS-D-17-0149.1

Park J, Choi M (2015) Estimation of evapotranspiration from ground-based meteorological data and global land data assimilation system (GLDAS). Stoch Environ Res Risk Assess 29(8): 1963-1992. https://doi.org/10.1007/s00477-014-1004-2

Penman HL (1948) Natural evaporation from open water, bare soil and grass. Proceedings of the Royal Society of London. Series A, Mathematical and Physical Sciences, 193(1032), 120-145. https://doi.org/10.1098/rspa.1948.0037

Pielke RA (2001) Influence of the spatial distribution of vegetation and soils on the prediction of cumulus convective rainfall. Rev. Geophys 39: 151 – 177. https://doi.org/10.1029/1999RG000072

Qu YP, Lyu J, Zhang WB, Su ZC, Li Z (2018) Progress in research on historical extreme drought in China. Adv Water Resour 29 (2): 283-292. doi: 10.14042/j.cnki.32.1309.2018.02.016

Rahmstorf S, Coumou D (2011) Increase of extreme events in a warming world. Proceedings of the National Academy of Sciences of the United States of America, 108 (44): 17905-17909. https://doi.org/10.1073/pnas.1101766108

Rana A, Moradkhani H, Qin Y (2017) Understanding the joint behavior of temperature and precipitation for climate change impact studies. Theor. Appl. Climatol 129(1-2):

321-339. https://doi.org/10.1007/s00704-016-1774-1

Renard B, Lang M (2007) Use of a Gaussian copula for multivariate extreme value analysis: Some case studies in hydrology. Adv Water Resour 30(4):897-912. https://doi.org/10.1016/j.advwatres.2006.08.001

Rodell M, Houser PR, Jambor U, Gottschalck J, Mitchell K, et al (2004) The global land data assimilation system. Bull Am Meteorol Soc 85(3): 381–394. https://doi.org/10.1175/BAMS-85-3-381

Salvadori G, Michele CD (2004) Frequency analysis via copulas: Theoretical aspects and applications to hydrological events.Water Resour. Res 40(12). https://doi.org/10.1029/2004WR003133

Sen PK (1968) Estimates of the regression coefficient based on Kendall's tau. J Am Stat Assoc 63:1379–1389. https://doi.org/10.1080/01621459.1968.10480934

Shiau JT (2006) Fitting drought duration and severity with two-dimensional copulas. Water Resour. Manag 20(5): 795-815. https://doi.org/10.1007/s11269-005-9008-9

Shiau JT, Modarres R (2009) Copula-based drought severity-duration-frequency analysis in Iran. Meteorol. Appl 16(4): 481-489. https://doi.org/10.1002/met.145

Sharma A, Goyal MK (2020) Assessment of drought trend and variability in India using wavelet transform. Hydrol Sci J 65(9): 1539-1554. https://doi.org/10.1080/02626667.2020.1754422

Sklar A (1959) Fonctions de répartition à n dimensions et leurs marges. Publ. Inst. Stat. Univ. Paris 8, 229–231. https://doi.org/10.1007/978-3-642-33590-7

Smirnov N (1948) Table for estimating the goodness of fit of empirical distributions.

Ann. Math. Stat. 19, 279–281.

Tang YH, Chen XH (2015) Multi-scale spatio-temporal characteristics and influence of precipitation variation in Zhujiang River basin during the last 50 years. Scientia Geographica Sinica, 35(4), 476-482.

Thilakarathne M, Sridhar V (2017) Characterization of future drought conditions in the Lower Mekong River Basin. Weather. Clim. Extremes 17: 47–58. https://doi.org/10.1016/j.wace.2017.07.004

Tomas-Burguera M, Vicente-Serrano SM, Peña-Angulo D, Domínguez-Castro F, Noguera I, El Kenawy A (2020) Global characterization of the varying responses of the standardized precipitation evapotranspiration index to atmospheric evaporative demand. J. Geophys. Res. Atmos. 125(17). https://doi.org/10.1029/2020JD033017

Trenberth KE, Dai A, Van Der Schrier G, Jones PD, Barichivich J, Briffa KR, Sheffield J (2014) Global warming and changes in drought. Nat Clim Chang 4(1), 17-22. https://doi.org/10.1038/nclimate2067

Vicente-Serrano SM (2016) Foreword: Drought complexity and assessment under climate change conditions. Cuadernos de investigación geográfica 42(1): 7-11. https://doi.org/10.18172/cig.2961

Wang LY, Yuan X, Xie ZH, Wu PL, Li YH (2016) Increasing flash droughts over China during the recent global warming hiatus. Sci. Rep 6, 30571. https://doi.org/10.1038/srep30571

Wang YM, Yuan X (2021) Anthropogenic speeding up of south China flash droughts as exemplified by the 2019 summer - autumn transition season. Geophys. Res. Lett.

48(9). https://doi.org/10.1029/2020GL091901

Wee P, Shitan M (2013) Modelling rainfall duration and severity using copula. Sri Lankan Journal of Applied Statistics, 14(1).

Wei J, Su H, Yang ZL (2016) Impact of moisture flux convergence and soil moisture on precipitation: a case study for the southern United States with implications for the globe. Clim. Dyn, 46: 467－481. https://doi.org/10.1007/s00382-015-2593-2

Wu CH, Hu BX, Huang G, Wang P, Xu K (2018) Responses of runoff to historical and future climate variability over China. Hydrol Earth Syst Sci 22:1971–1991. https://doi.org/10.5194/hess-22-1971-2018

Wu CH, Yeh PJF, Chen YY, Lv WH, Hu BX, Huang GR (2021) Copula-based risk evaluation of global meteorological drought in the 21st century based on CMIP5 multi-model ensemble projections. J. Hydrol. 598. https://doi.org/10.1016/j.jhydrol.2021.126265

Xia J, Wei S (2016) Perspective on water security issue of changing environment in China. J. Hydraul. Eng 47(3): 292-301.

Xu K, Yang DW, Xu XY, Lei HM (2015) Copula based drought frequency analysis considering the spatio-temporal variability in Southwest China. J. Hydrol 527: 630-640. https://doi.org/10.1016/j.jhydrol.2015.05.030

Yan D, Ren L, Wang G, Lin Q, Xiao W, Qin T (2016) Initiatives on evolution of terrestrial water cycle and its role in global change. Adv Water Resour 27(6): 935-942.

Yevjevich VM (1967) An objective approach to definitions and investigations of continental hydrologic droughts. Hydrol. Pap. Colorado State Univ. no. 23.

Yin YH, Ma DY, Wu SH, Pan T (2015) Projections of aridity and its regional variability over China in the mid-21st century. Int J Climatol 35(14): 4387-4398. https://doi.org/10.1002/joc.4295

Yuan X, Wang L, Wu P, Ji P, Sheffield J, Zhang M (2019) Anthropogenic shift towards higher risk of flash drought over China. Nat. Commun.10(1):1-8. https://doi.org/10.1038/s41467-019-12692-7

Zhang L, Singh VP (2007) Bivariate rainfall frequency distributions using Archimedean copulas. J. Hydrol, 332(1-2), 93-109. https://doi.org/10.1016/j.jhydrol.2006.06.033

Zhang Q, Xiao MZ, Singh VP, Chen XH (2013) Copula-based risk evaluation of hydrological droughts in the East River basin, China. Stoch Environ Res Risk Assess 27(6): 1397-1406. https://doi.org/10.1007/s00477-012-0675-9

Zhang YQ, You QL, Chen CC, Jing G, Adnan M (2018) Evaluation of downscaled CMIP5 coupled with VIC model in simulating flash droughts in a humid subtropical basin, China. J. Clim 31(31): 1075-1090. https://doi.org/10.1175/JCLI-D-17-0378.1

Zhang HY, Wu CH, Hu, BX (2019) Recent intensification of short-term concurrent hot and dry extremes over the Pearl River basin, China. Int J Climatol 39: 4924-4937. https://doi.org/10.1002/joc.6116

Zhu Y, Liu Y, Wang W, Yuan F, Ma MW, Yin YX (2021) Analysis of spatial-temporal characteristics of flash drought and slowly-evolving drought using soil moisture percentile. Transactions of the Chinese Society of Agricultural Engineering (Transactions of the CSAE), 37(2): 114-122.

Figures and tables

Table 1. Univariate marginal distribution functions used in this study.

Table 2. Archimedean Copulas used in this study. u and v are the marginal distribution functions; θ denotes the parameter of Copula.

Table 3. The design values of FD characteristics and their joint return periods in three basins.

Fig. 1 The location of the Pearl River basin and the distribution of meteorological stations.

Fig. 2 Spatial distributions of (a) the number of FD occurrences and mean (b) *D* (in days), (c) *I*, and (d) *P* over the PRB during 1953-2013.

Fig. 3 Spatial distributions of the trend magnitudes in (a) *D* (in days), (b) *I*, and (c) *P* over the PRB during 1953-2013. Significant increasing (decreasing) trends (p<0.05) are denoted by white regular triangles (green inverted triangles).

Fig. 4 Spatial distributions of the best-fitted marginal distribution functions of (a) *D,* (b) *I,* and (c) *P* as well as the best-fitted copula functions of (d) *D-I,* (e) *D-P,* and (f) *P-I* over the PRB.

Fig. 5 Two-dimensional joint distribution maps of *D-I, D-P,* and *P-I* in WRB (the first row), NRB (the second row), and ERB (the third row).

Fig. 6 The contour maps of the joint return period (T_o) (in years) of *D-I, D-P,* and *P-I* in WRB (the first row), NRB (the second row), and ERB (the third row).

Fig. 7 Spatial distributions of T_o (in years) of (a) *D1-I1,* (b) *D2-I2,* (c) *D3-I3*, (d) *D1-P1,* (e) *D2-P2,* (f) *D3-P3*, (g) *I1-P1,* (h) *I2-P2,* and (i) *I3-P3* over the PRB.

Fig. 8 The contour maps of the joint return period (T_a) (in years) of *D-I, D-P,* and *P-I* in WRB (the first row), NRB (the second row), and ERB (the third row).

Fig. 9 Spatial distributions of T_a (in years) of (a) *D1-I1,* (b) *D2-I2,* (c) *D3-I3*, (d) *D1-P1,* (e) *D2-P2,* (f) *D3-P3*, (g) *I1-P1,* (h) *I2-P2,* (i) *I3-P3* over the PRB.

Table 1. Univariate marginal distribution functions used in this study.

Distribution	PDF	Parameter
Gamma	$F(x)=\dfrac{\beta^{-\alpha}}{\Gamma(\alpha)}\int_0^x t^{\alpha-1}e^{-t/\beta}dt$	α , β
Exponential	$F(x)=1-\exp(-(x-\xi)/\alpha)$	α , ξ
GEV	$F(x)=\exp\left(-\exp\left(k^{-1}\ln\left(1-\dfrac{k(x-\xi)}{\alpha}\right)\right)\right)$	α , ξ , k
Lognormal	$F(x)=\dfrac{1}{x\sigma\sqrt{2\pi}}\exp\left\{-\dfrac{(\ln x-\mu)^2}{2\sigma^2}\right\}$	σ , μ

Table 2. Archimedean Copulas used in this study. u and v are the marginal distribution functions; θ denotes the parameter of Copula.

Copulas	Function	Range
Clayton	$\max\left(\left[u^{-\theta}+v^{-\theta}-1\right]^{-1/\theta},0\right)$	(0,∞)
Frank	$-\frac{1}{\theta}\ln[1+\frac{(\mathrm{e}^{-\theta u}-1)(\mathrm{e}^{-\theta v}-1)}{(\mathrm{e}^{-\theta}-1)}]$	(-∞,∞)
Gumbel	$\exp\left(-\left[(-\ln u)^{\theta}+(-\ln v)^{\theta}\right]\right)^{1/\theta}$	[1,∞)

Table 3. The design values of FD characteristics and their joint return periods in three basins.

Basins	T/a	Do/d	Io	Po	Do-Io		Do-Po		Po-Io	
					T_o/a	T_a/a	T_o/a	T_a/a	T_o/a	T_a/a
WRB	10	18.84	0.57	0.78	9.70	10.32	9.63	10.39	9.84	10.16
	20	21.70	0.61	0.99	16.13	26.31	15.70	27.55	17.57	23.22
	50	23.61	0.63	1.15	32.34	110.17	31.51	120.97	35.85	82.58
	100	24.72	0.65	1.25	57.86	368.15	56.84	415.31	62.62	248.14
NRB	10	20.70	0.69	1.17	6.26	24.84	7.47	15.12	9.49	10.57
	20	21.29	0.74	1.24	11.28	88.30	12.79	45.91	17.66	23.05
	50	21.90	0.79	1.32	26.30	505.98	28.02	231.96	37.75	74.03
	100	22.29	0.82	1.38	51.31	1959.7	53.11	853.84	66.16	204.70
ERB	10	23.44	0.78	1.30	7.16	16.57	6.85	18.49	8.61	11.93
	20	24.81	0.84	1.36	12.67	47.41	12.22	55.15	15.41	28.47
	50	26.34	0.89	1.43	28.13	224.65	27.52	272.87	32.62	107.07
	100	27.37	0.93	1.46	53.33	801.30	52.65	993.99	58.83	333.19

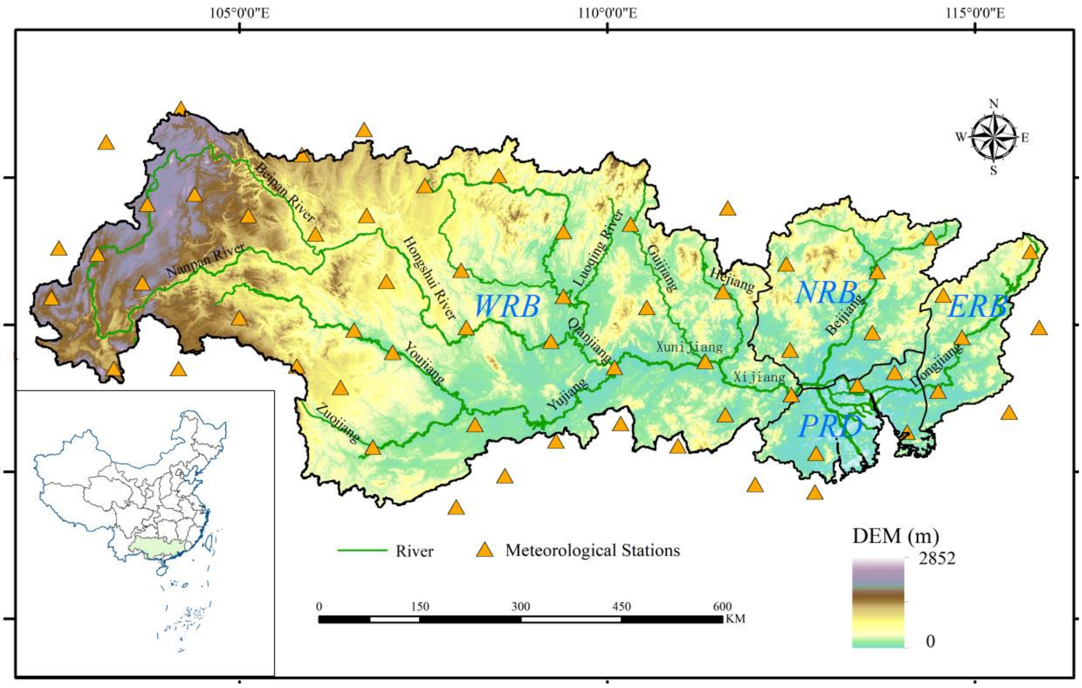

Fig. 1 The location of the Pearl River basin and the distribution of meteorological stations

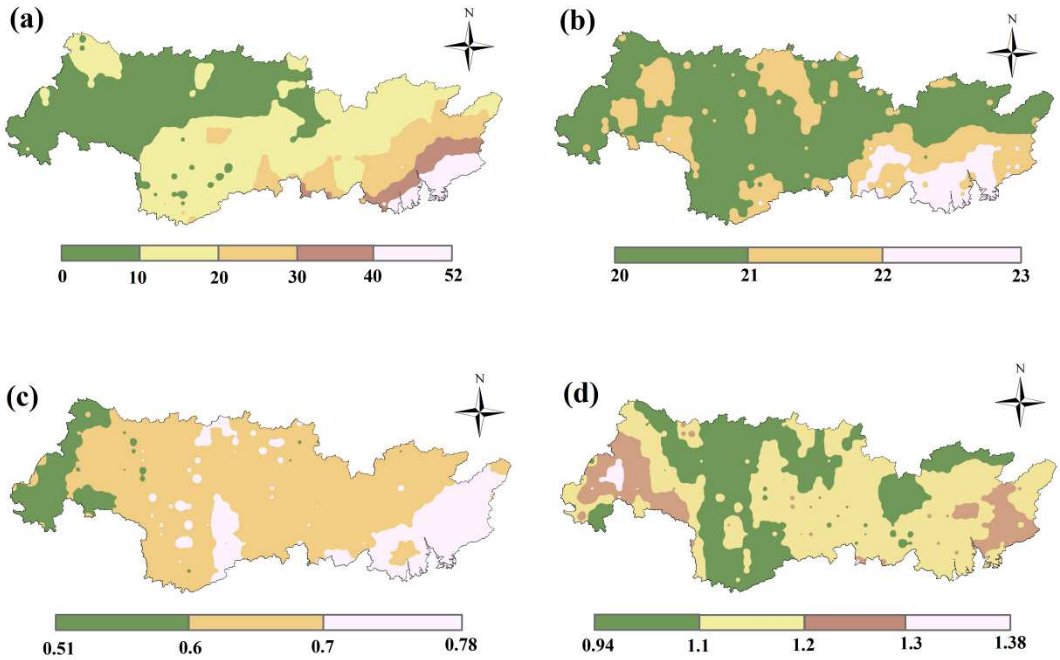

Fig. 2 Spatial distributions of (a) the number of FD occurrences and mean (b) *D* (in days), (c) *I*, and (d) *P* over the PRB during 1953-2013

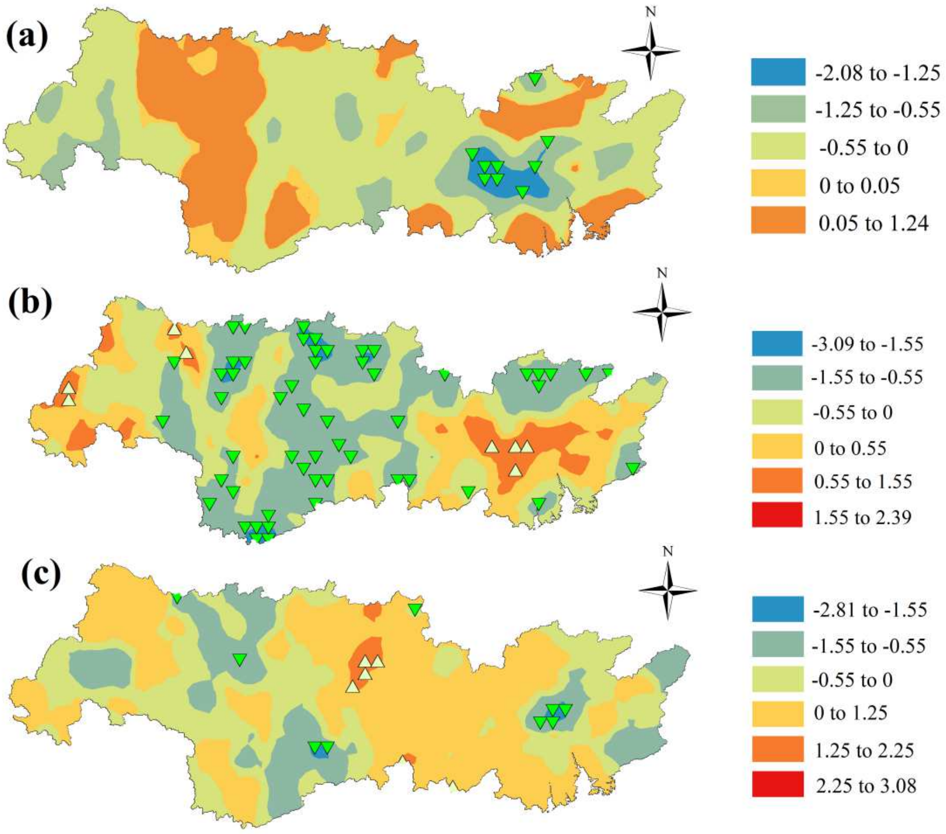

Fig. 3 Spatial distributions of the trend magnitudes in (a) *D* (in days), (b) *I*, and (c) *P* over the PRB during 1953-2013. Significant increasing (decreasing) trends (p<0.05) are denoted by white regular triangles (green inverted triangles)

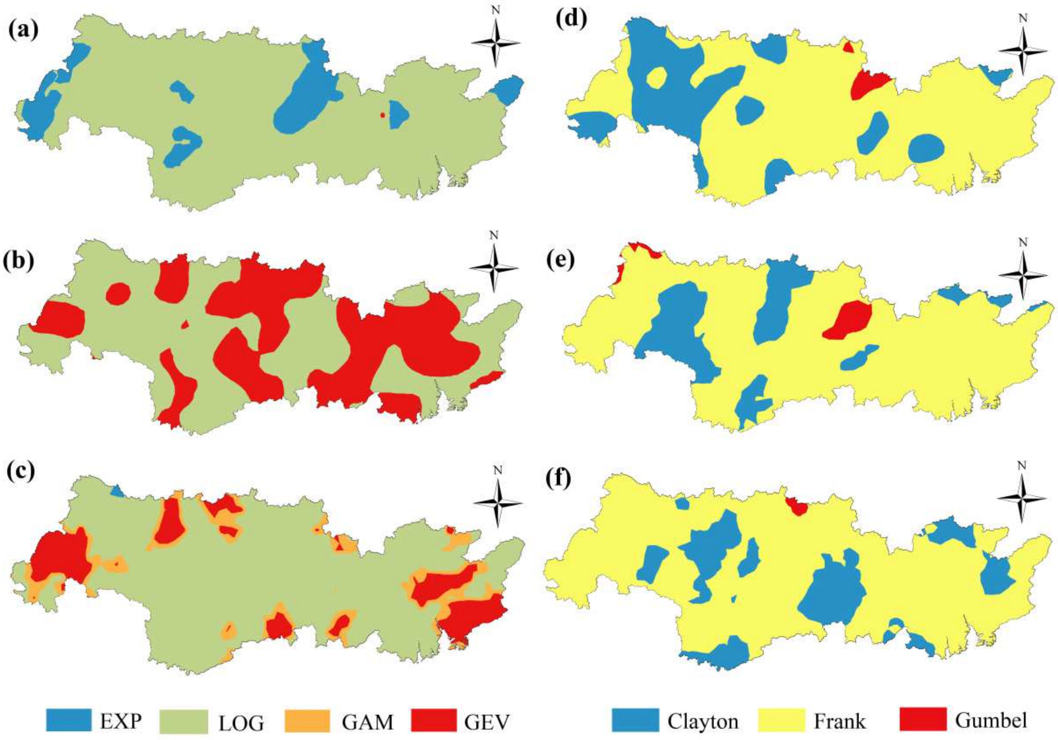

Fig. 4 Spatial distributions of the best-fitted marginal distribution functions of (a) *D*, (b) *I*, and (c) *P* as well as the best-fitted copula functions of (d) *D-I*, (e) *D-P*, and (f) *P-I* over the PRB

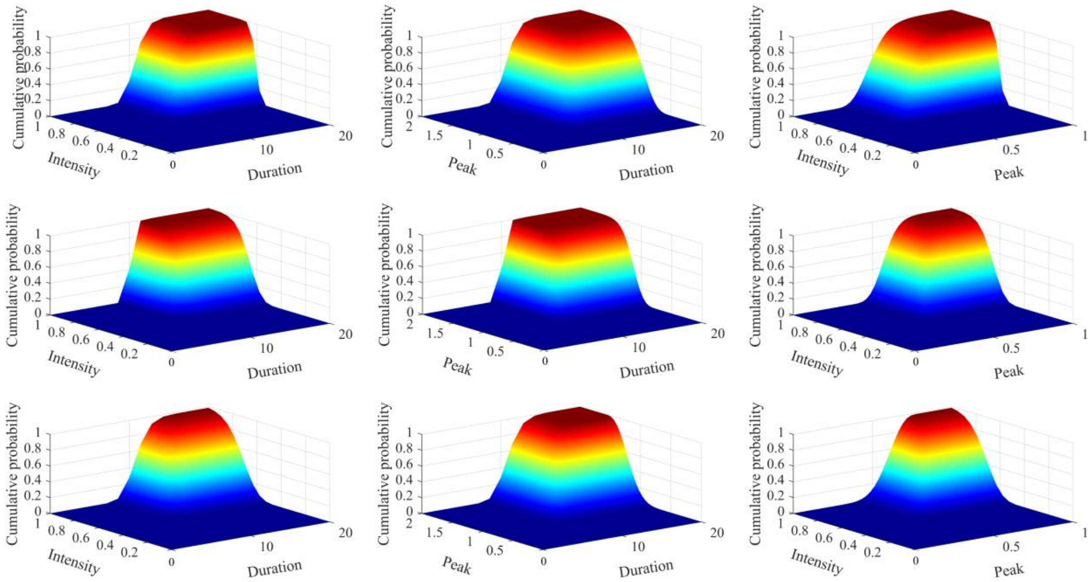

Fig. 5 Two-dimensional joint distribution maps of *D-I, D-P,* and *P-I* in WRB (the first row), NRB (the second row), and ERB (the third row)

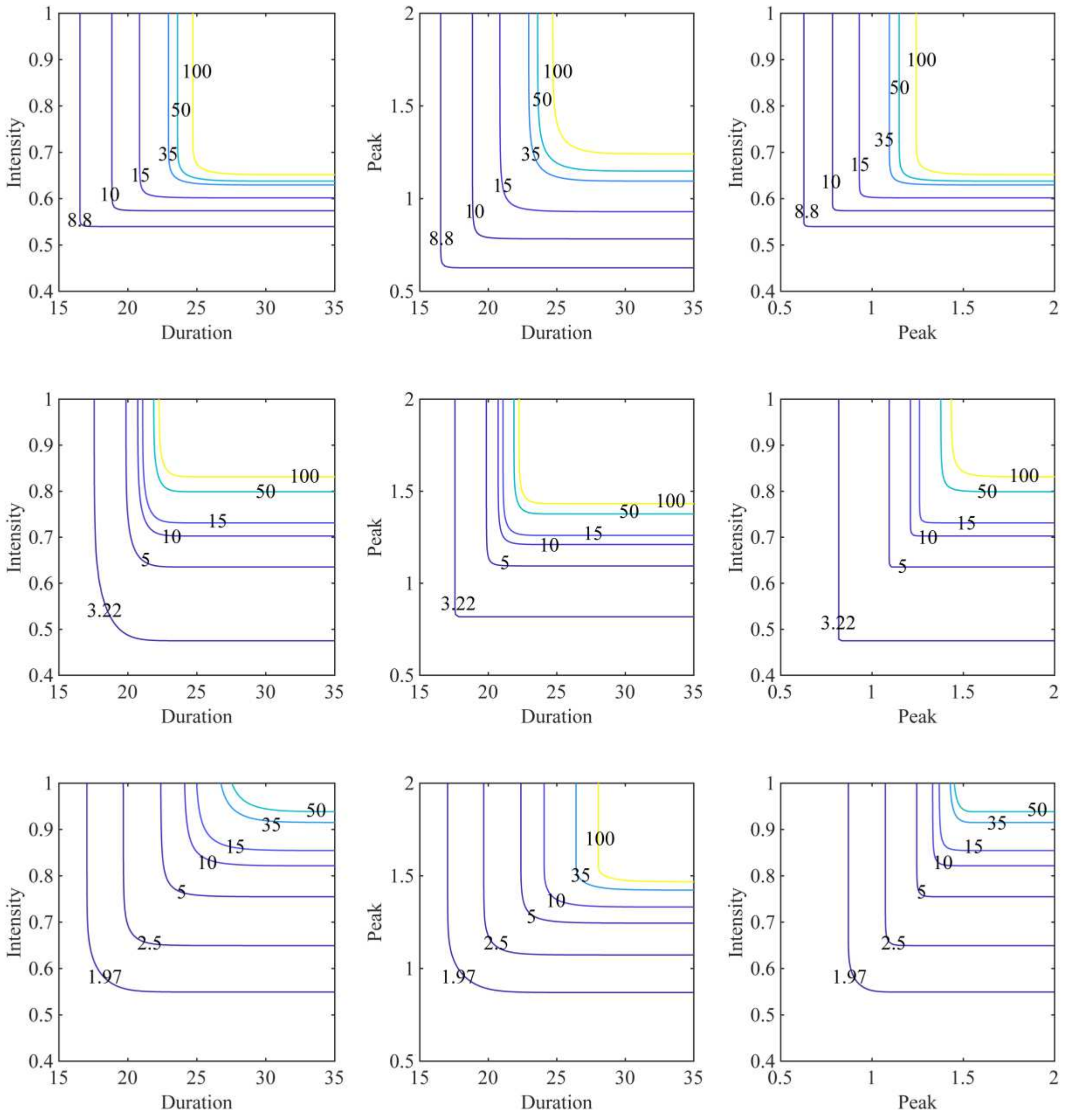

Fig. 6 The contour maps of the joint return period (T_o) (in years) of *D-I, D-P,* and *P-I* in WRB (the first row), NRB (the second row), and ERB (the third row)

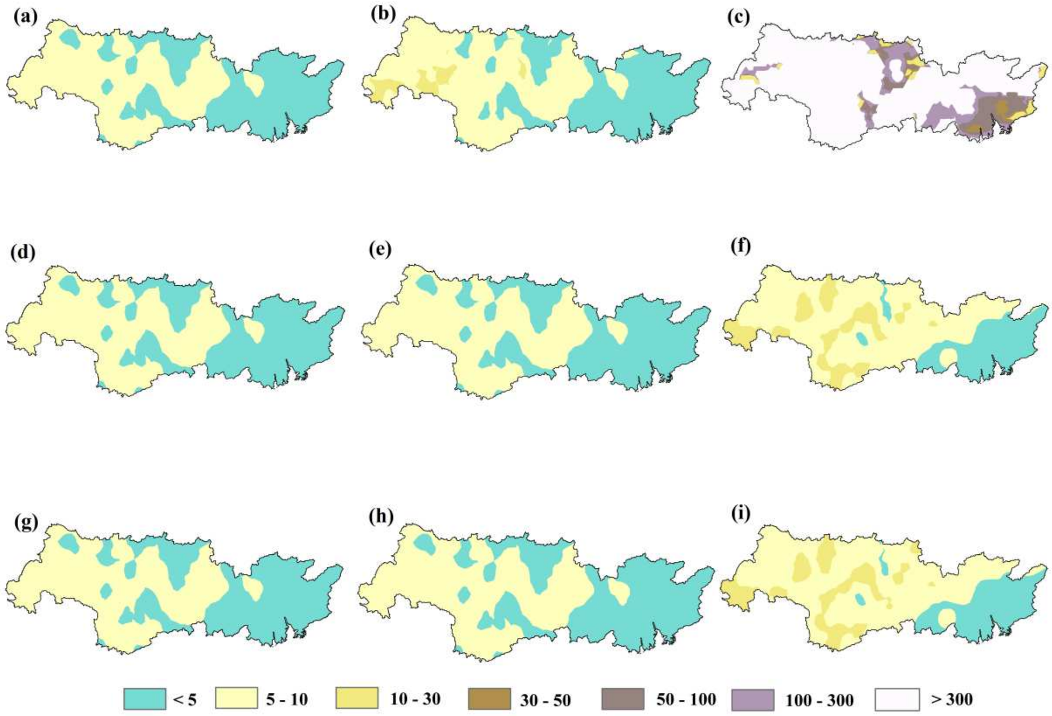

Fig. 7 Spatial distributions of T_o (in years) of (a) *D1-I1,* (b) *D2-I2,* (c) *D3-I3*, (d) *D1-P1,* (e) *D2-P2,* (f) *D3-P3*, (g) *I1-P1,* (h) *I2-P2,* and (i) *I3-P3* over the PRB

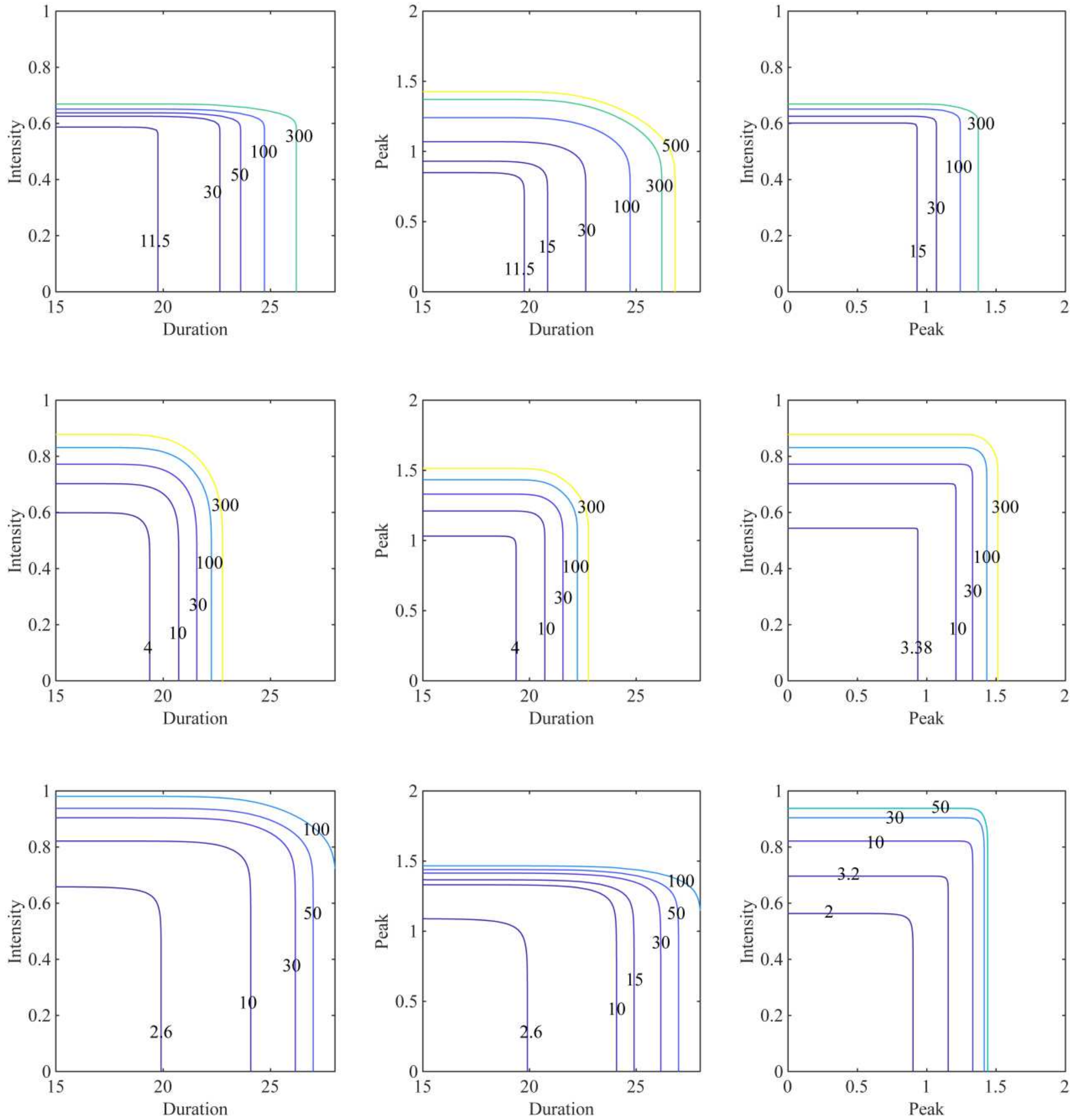

Fig. 8 The contour maps of the joint return period (T_a) (in years) of *D-I, D-P,* and *P-I* in WRB (the first row), NRB (the second row), and ERB (the third row)

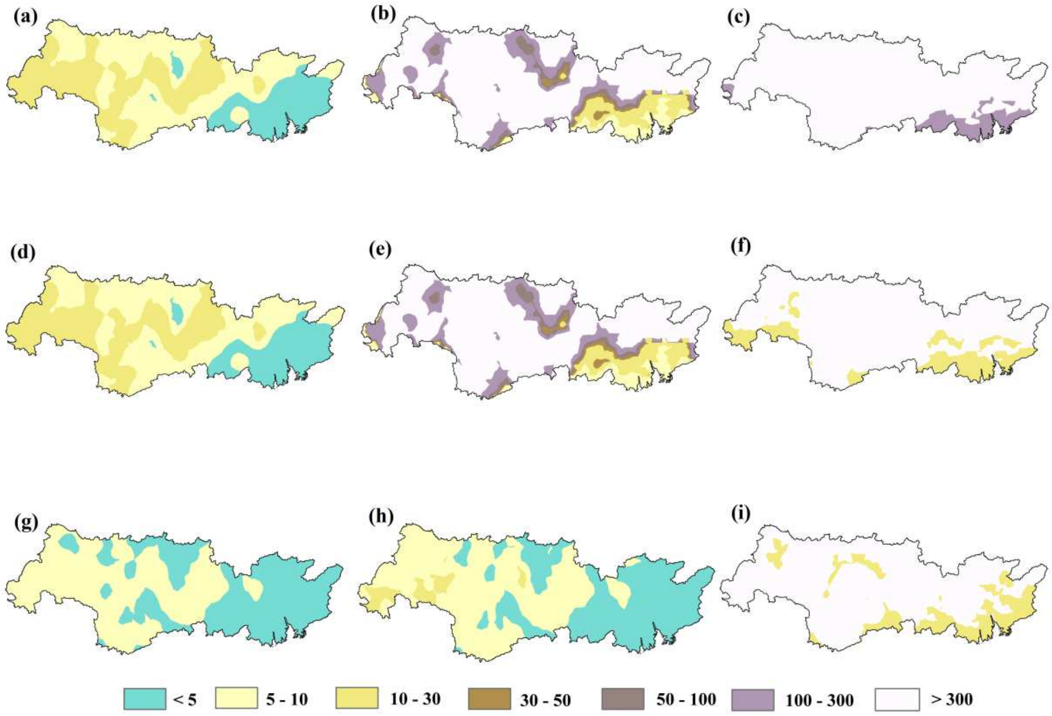

Fig. 9 Spatial distributions of T_a (in years) of (a) *D1-I1,* (b) *D2-I2,* (c) *D3-I3*, (d) *D1-P1,* (e) *D2-P2,* (f) *D3-P3*, (g) *I1-P1,* (h) *I2-P2,* (i) *I3-P3* over the PRB.